

# Wider Voltage Window, High Capacity and Ultra-Long Life of an $\text{Na}_{0.91}\text{MnO}_2$ Cathode for an Aqueous High-Performance Supercapacitor

Tianfeng Qin\*<sup>[a, b]</sup>

The potential window of an aqueous supercapacitor cathode is usually less than 1.3 V, which hinders the enhancement of the energy density and can be conquered by activating the multiple redox reactions of the cathode. Herein, tetragonal phase  $\text{Na}_{0.91}\text{MnO}_2$  nanosheets/nanowires arrays with high cation content are produced *in situ* on an electrochemically treated carbon cloth by an electrochemical oxidation method. It is observed that the  $\text{Na}_{0.91}\text{MnO}_2$  nanosheet/hanowire array electrode can operate stably within the potential window of  $-0.6$  V to  $1.2$  V (vs Ag/AgCl) with an ultrahigh capacity of  $856 \text{ C g}^{-1}$  and

an outstanding stability and excellent rate ability. With a carbon fiber fabric with a large surface area as the anode, the  $\text{Na}_{0.91}\text{MnO}_2$  cathode in the two-electrode cell can still operate stably within the voltage range from 0 to 2.07 V (still within the range of the three redox peak couples, demonstrating a high energy density of  $138 \text{ Wh kg}^{-1}$ , an excellent power density of  $33 \text{ kW kg}^{-1}$  as well as 100% retention even after 120000 cycles. This work may pave the way for the development of an aqueous supercapacitor cathode with a wider potential window.

## 1. Introduction

With the significant advantages of safety, high power input/output and long life span,<sup>[1–7]</sup> the aqueous supercapacitors (ASCs) have gained much attention recent years. But ASCs suffer from the low energy density (E) due to the narrow stable work voltage window (V) according to the equation of  $E=CV^2/2$ . The low voltage window is limited by the low theoretical decomposition of water (1.23 V), which can be expanded by the two methods reported in literatures.<sup>[8]</sup> One is to use the aqueous electrolyte called “water-in-salt”, which could construct the interphase at the interface of electrode/electrolyte. Moreover, lower the content and chemical activity of free water molecules through the strong coordination of almost all water molecules to lithium ions and the formation of lithium ion solvation sheath.<sup>[9–11]</sup> But the ultrahigh cost of salt (LiTFSI) in “water-in-salt” greatly limits the wide application. The other is to enhance the over-potential of the hydrogen and oxygen evolution reactions of the aqueous electrolyte.<sup>[8,12]</sup> Most of electrode materials show the low over-potential, resulting in the oxygen/hydrogen evolution and the narrow potential range of electrode materials.<sup>[13,14]</sup> In order to achieve the high-voltage

ASCs, it is urgent to design and fabricate the positive electrode materials with the wide potential window through increasing the over-potential of oxygen evolution reaction (OER).

Among the various electrode materials, the manganese dioxide ( $\text{MnO}_2$ ) has attracted much attention due to the high theoretical specific capacitance, abundant reserves and environment friendly.<sup>[15–17]</sup> More importantly,  $\text{MnO}_2$  shows the high over-potential of OER in the aqueous electrolyte but works within the narrow potential range from 0 V to 1 V in most cases.<sup>[18–20]</sup> In recent years, a few research reports that  $\text{MnO}_2$  can work stably within the wide potential window from 0 V to 1.3 V by activating the multiple redox reactions at about 1 V,<sup>[12,21, 22]</sup> in which  $\text{Na}^+$  intercalates into  $\text{MnO}_2$  and reversibly de-intercalates from  $\text{MnO}_2$ .<sup>[23,24]</sup> Although working within the potential window of 0 V to 1.3 V,  $\text{MnO}_2$  shows the unsatisfactory capacity property and lifespan due to the poor reversibility and the structural instability, especially in long-term cycle at the large current. In order to overcome the challenges mentioned above, the strategy of the pre-insertion of alkaline cations (e.g.  $\text{Na}^+$  and  $\text{K}^+$ ) into  $\text{MnO}_2$  are used to improve the capacity and lifespan,<sup>[12,21, 25]</sup> which can increase the number of redox couple of  $\text{Mn}^{3+}/\text{Mn}^{4+}$  and be used as the pillar in the interlayers to ensure the structural stability. The cation ratio (cation/Mn) inserted in  $\text{MnO}_2$  is low and the potential window of  $\text{MnO}_2$  is less than 1.3 V,<sup>[26,27]</sup> which greatly hinder the enhancement of the electrochemical properties. Thus, it is a challenge to insert the higher content of cation and operate in the wider potential window for  $\text{MnO}_2$ .

Recently, the transition of  $\text{Mn}_3\text{O}_4$  into  $\text{Na}_{0.5}\text{MnO}_2$  induced by the electrochemical oxidation method attracts a wide attention with the high content of cation up to 0.5 but  $\text{Na}_{0.5}\text{MnO}_2$  just works within the narrow potential window of 0 V to 1.3 V with one or two couple of redox reactions (about 0.65 V and about 1 V).<sup>[12]</sup> Teng group reports that  $\text{Mn}_3\text{O}_4$  can charge/discharge

[a] Dr. T. Qin

National & Local Joint Engineering Laboratory for Optical Conversion Materials and Technology

School of Physical Science and Technology  
Lanzhou University, Lanzhou 730000 (P.R. China)

E-mail: qintf17@lzu.edu.cn

[b] Dr. T. Qin

School of Physical Science and Technology  
Key Laboratory for Magnetism and Magnetic Materials of the Ministry of Education  
Lanzhou University, Lanzhou, 730000 (China)

 Supporting information for this article is available on the WWW under <https://doi.org/10.1002/batt.201900096>

within  $-0.5$  V to  $1.1$  V (vs Ag/AgCl) in  $\text{Na}_2\text{SO}_4$  aqueous electrolyte (one at about  $1$  V for charging peak and the other at  $-0.25$  V for discharging peak).<sup>[28]</sup> Inspired by the reports mentioned above, could we activate the multiple redox reaction of the manganese oxides to further expand the work potential window? Herein, the high cation content of  $\text{Na}_{0.91}\text{MnO}_2$  nanosheets/nanowires arrays were in-situ produced on the electrochemically treated carbon cloth (ECC) derived from the transition of  $\text{MnO}/\text{Mn}_3\text{O}_4$  induced by the electrochemical oxidation. The high cation content can induce the much more redox couple of  $\text{Mn}^{3+}/\text{Mn}^{4+}$ , leading to the enhancement of specific capacitance to  $856 \text{ Cg}^{-1}$  at  $1 \text{ Ag}^{-1}$  and the excellent rate ability in the three-electrode configuration. And  $\text{Na}_{0.91}\text{MnO}_2$  nanosheets/nanowires arrays on ECC as the electrode material can operate stably within the wide potential window of  $-0.6$  V to  $1.2$  V (vs Ag/AgCl) and shows three couple of redox peaks even after 10000 cycles. A two-electrode cell configuration based on  $\text{Na}_{0.91}\text{MnO}_2$  as the cathode and the carbon fiber fabric with large surface area as the anode is employed to further demonstrate the advantage of the wide potential window, in which the carbon fiber fabric anode plays the role of reference electrode and counter electrode. It is more surprising that  $\text{Na}_{0.91}\text{MnO}_2$  nanosheets/nanowires arrays can operate stably within the voltage range from  $0$  to  $2.07$  V also with the three couple of redox peaks, delivering the high energy density of  $138 \text{ Wh kg}^{-1}$  and the excellent power density  $33 \text{ kW kg}^{-1}$  based on the active material of  $\text{Na}_{0.91}\text{MnO}_2$ . Moreover,  $100\%$  retention of the initial capacity is obtained after 120000 cycles at a high current density of  $27 \text{ Ag}^{-1}$ .

## 2. Results and Discussion

$\text{MnO}/\text{Mn}_3\text{O}_4$  was electrodeposited firstly on ECC using the chronoamperometry technique (see Figure S1 in the Supporting Information). The electrochemical properties of  $\text{MnO}/\text{Mn}_3\text{O}_4$  were tested (Figure S2), demonstrating the poor cycle stability of less than  $50\%$  after 10000 cycles. The rapid decrease of the capacity in the initial 650 cycles is due to the dissolution of  $\text{Mn}^{2+}$  into the electrolyte according to Jahn-Teller effect,<sup>[29]</sup> in which  $\text{Mn}^{2+}$  is derived from the reduction of  $\text{Mn}^{3+}$  together with the oxidation of  $\text{Mn}^{3+}$  into  $\text{Mn}^{4+}$ . In order to transform  $\text{MnO}/\text{Mn}_3\text{O}_4$  into  $\text{Na}_{0.91}\text{MnO}_2$  using Jahn-Teller effect, the electrochemical oxidation method is carried out on  $\text{MnO}/\text{Mn}_3\text{O}_4$  (Figure S3). The capacity of  $\text{MnO}/\text{Mn}_3\text{O}_4$  electrode gradually decreases and becomes stable. The clear electrolyte changes into the earthy yellow after the electrochemical oxidation due to the dissolution of  $\text{Mn}^{2+}$  (Figure S3c and d). X-ray diffraction (XRD) patterns of  $\text{MnO}/\text{Mn}_3\text{O}_4$  (black spectra line) and  $\text{Na}_{0.91}\text{MnO}_2$  (red spectra line) exhibit the obvious signal peaks (about  $25^\circ$  and  $44^\circ$ ) of ECC substrate denoted as C (Figure 1a). As for the black pattern, two types of signal peaks are observed and belong to the face-centered cubic  $\text{MnO}$  (JCPDS 01-1206) and the tetrahedral hausmannite  $\text{Mn}_3\text{O}_4$  (JCPDS 24-0734), which is consistent with the previously reported patterns of  $\text{MnO}$  and  $\text{Mn}_3\text{O}_4$ .<sup>[12,30]</sup> With regard to the red spectra line, excluding the peaks of C, the diffraction peaks

are indexed as the crystal plane (010), (101) and (050) of orthorhombic phase  $\text{Na}_{0.91}\text{MnO}_2$  (PDF 38-0965), which is previously reported in sodium ion battery.<sup>31</sup> Raman characterization was made to further confirm the phase of  $\text{Na}_{0.91}\text{MnO}_2$  (Figure S4). Raman spectra of  $\text{Na}_{0.91}\text{MnO}_2$  presents the obvious Raman bands centered at  $589 \text{ cm}^{-1}$ ,  $511 \text{ cm}^{-1}$  and  $283 \text{ cm}^{-1}$ , which is consistent with the previous reports on Li and Na-Birnessite  $\text{MnO}_2$ .<sup>[12,32,33]</sup> X-ray photoelectron spectroscopy (XPS) is employed to analysis the variations of the value state and the bonding in the samples of  $\text{MnO}/\text{Mn}_3\text{O}_4$  and  $\text{Na}_{0.91}\text{MnO}_2$  (Figure 1b). For  $\text{MnO}/\text{Mn}_3\text{O}_4$ , the black spectrum shows the existence of C, O and Mn elements.<sup>[34,35]</sup> After the electrochemical oxidation, the red spectral line of  $\text{Na}_{0.91}\text{MnO}_2$  exhibits the presence of C, O, Mn and Na elements.<sup>[34-36]</sup> The signal peaks of C in XPS spectra are derived from ECC substrate and Na from the insertion of  $\text{Na}^+$  in  $1 \text{ M } \text{Na}_2\text{SO}_4$  solution into  $\text{MnO}_2$ . The narrow spectra of Mn2p for  $\text{MnO}/\text{Mn}_3\text{O}_4$  and  $\text{Na}_{0.91}\text{MnO}_2$  were recorded to investigate the value state of elements (Figure 1c). For  $\text{MnO}/\text{Mn}_3\text{O}_4$ , Mn2p<sub>3/2</sub> and Mn2p<sub>1/2</sub> peaks are fitted into four peaks  $642.22 \text{ eV}$  and  $640.18 \text{ eV}$ ,  $652.44 \text{ eV}$  and  $655.70 \text{ eV}$ , which is consistent with  $\text{Mn}^{3+}$  and  $\text{Mn}^{2+}$ .<sup>[30]</sup> After the electrochemical oxidation, Mn2p narrow spectrum for  $\text{Na}_{0.91}\text{MnO}_2$  shows four peaks with the binding energy at  $642.90 \text{ eV}$  and  $641.86 \text{ eV}$ ,  $654.57 \text{ eV}$  and  $653.10 \text{ eV}$ , corresponding to  $\text{Mn}^{4+}$  and  $\text{Mn}^{3+}$ .<sup>[37]</sup> For the core-level O1s spectra (Figure 1d), both  $\text{MnO}/\text{Mn}_3\text{O}_4$  and  $\text{Na}_{0.91}\text{MnO}_2$  show three peaks at the binding energy of  $530.11 \text{ eV}$ ,  $531.49 \text{ eV}$  and  $532.79 \text{ eV}$ , which is consistent with Mn–O, Mn–OH and –OH from adsorbed water.<sup>[35,38]</sup> The narrow spectra of Na1s (Figure 1e) shows the binding energy at  $1071.06 \text{ eV}$ , corresponding to the bond of  $-\text{O}$ .<sup>[36]</sup> In CV and GCD processes (charge to  $1.3 \text{ V}$ ),  $\text{Mn}^{2+}$  in  $\text{MnO}$  and the tetrahedral centers dissolved into electrolyte and  $\text{Mn}^{3+}$  transforms into  $\text{Mn}^{4+}$  together with the rearrangement of  $\text{MnO}_6$  tetrahedral accompanied with the intercalation of water molecules.<sup>[12]</sup>  $\text{Na}^+$  are intercalated into the interlayers in the anodic process (discharging) confirmed by Na1s narrow spectra, leading to the formation of the tetragonal phase  $\text{Na}_{0.91}\text{MnO}_2$  and the high ratio of  $\text{Mn}^{3+}/\text{Mn}^{4+}$  up to  $0.91$ . Scanning electron microscopy (SEM) characterization is carried out to detect the morphology variations. SEM image indicates that the carbon fibers are evenly coated by the amount of  $\text{MnO}/\text{Mn}_3\text{O}_4$  nano-sheets (Figure 1f). Enlarged SEM image shows that the interconnected thin nano-sheets are almost vertically anchored on the surface of the carbon fiber (Figure 1g). After the electrochemical oxidation, the morphology of  $\text{Na}_{0.91}\text{MnO}_2$  changes into the interconnected nanosheets and some nanoclusters are adhered to the top of interconnected nanosheets (Figure 1h).

The more detail morphology variations of  $\text{MnO}/\text{Mn}_3\text{O}_4$  and  $\text{Na}_{0.91}\text{MnO}_2$  were further investigated by the transmission electron microscopy (TEM) (Figure 2). TEM image of  $\text{MnO}/\text{Mn}_3\text{O}_4$  displays the morphology of the irregular nanosheet (Figure 2a). The partially enlarged edge of the nanosheet exhibits that the nanosheet is composed of the interconnected nanowires with the diameter ranging from  $10 \text{ nm}$  to  $50 \text{ nm}$ , exposing the porous structure between nanowires (Figure 2b). The high-resolution transmission electron microscopy (HRTEM)

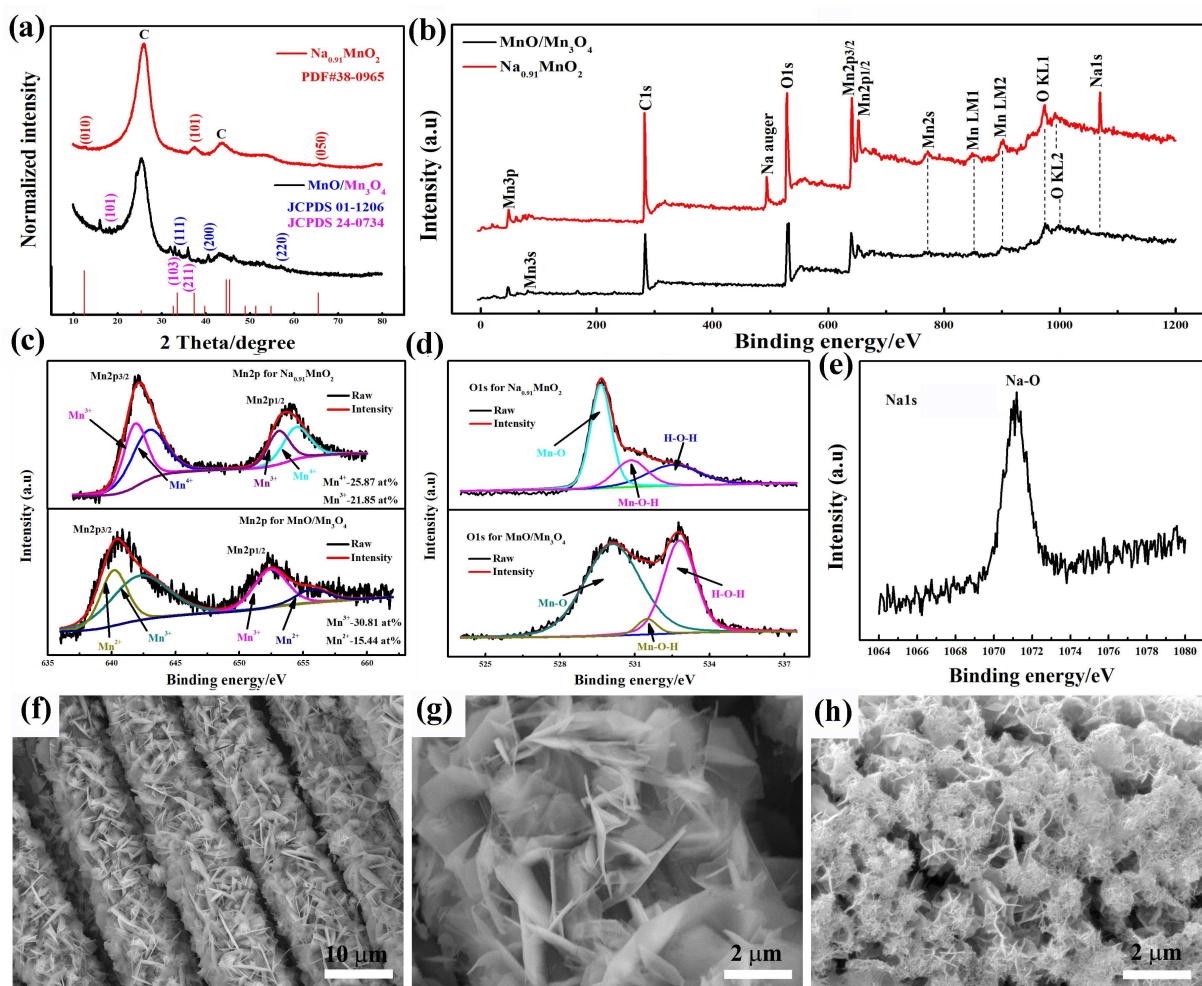


**Figure 1.** Characterization of  $\text{MnO}/\text{Mn}_3\text{O}_4$  and  $\text{Na}_{0.91}\text{MnO}_2$  on ECCs. (a) XRD patterns; (b) XPS spectra; (c) Mn2p narrow spectra; (d) O1s narrow spectra; (e) Na1s narrow spectra; (f) SEM image of  $\text{MnO}/\text{Mn}_3\text{O}_4$  on ECC and (g) corresponding enlarged SEM image; (h) SEM image of  $\text{Na}_{0.91}\text{MnO}_2$  on ECC.

image of single  $\text{MnO}/\text{Mn}_3\text{O}_4$  nanowire presents the clear lattice diffraction fringes with the spacing of 0.48 nm and 0.29 nm (Figure 2c), which are consistent with the (101) plane of tetrahedral  $\text{Mn}_3\text{O}_4$  marked by a series of red dots and the (111) plane of the face-centered cubic  $\text{MnO}$  highlighted by a series of green dots. The corresponding Fast Fourier Transform (FFT) pattern was collected (Figure 2d). The diffraction spots with the nature of single crystalline marked by the dashed red/green circles are in agreement with  $\text{Mn}_3\text{O}_4$  and  $\text{MnO}$  phases, respectively, which are consistent with the results of XRD and XPS characterizations. The coexistence of  $\text{Mn}_3\text{O}_4$  and  $\text{MnO}$  confirmed by FFT is also reported by Xiong group.<sup>[30]</sup> TEM images of  $\text{Na}_{0.91}\text{MnO}_2$  at the high and low magnifications were recorded (Figure 2e and f), respectively. Compared to  $\text{MnO}/\text{Mn}_3\text{O}_4$ , TEM image of  $\text{Na}_{0.91}\text{MnO}_2$  shows the nanosheet morphology but with the building blocks that compose of nanosheets, in which the top edge of nanosheet is connected by the nanowires array. Well-defined lattice diffraction fringe with the spacing 0.24 nm is observed (Figure 2g), corresponding to the (101) plane of  $\text{Na}_{0.91}\text{MnO}_2$  (XRD). FFT as the inset in the bottom right corner from Figure 2(g) shows the combination of the diffraction spots and rings, demonstrating the

features of single crystalline and polycrystalline. A typical HADDF-STEM image of  $\text{Na}_{0.91}\text{MnO}_2$  and the corresponding EDS elements mappings for Mn, O and Na are collected (Figure 2h). Elements of Mn, O and Na are distributed evenly through the whole nanosheet and nanowires, indicating the insertion of Na is homogeneous. Besides, the selected area electron diffraction (SAED) was carried out to uncover the nature of the crystallization (Figure S5). The SAED image of  $\text{MnO}/\text{Mn}_3\text{O}_4$  presents the combination of the diffraction spots of single crystal and the polycrystalline of the homocentric circles (Figure S5a). But SAED image of  $\text{Na}_{0.91}\text{MnO}_2$  shows the polycrystalline of the homocentric circles, indicating the decreased crystalline (Figure S5b).

The electrochemical properties of  $\text{Na}_{0.91}\text{MnO}_2$  are evaluated using a three-electrode configuration with 60 mL of 1 M  $\text{Na}_2\text{SO}_4$  electrolyte at room temperature. The electrochemical behavior of  $\text{Na}_{0.91}\text{MnO}_2$  is firstly investigated by CV at 10 mV s<sup>-1</sup>. CV curve shows three couple of redox peaks within the wide potential window from -0.6 V to 1.2 V (Figure 3a). In order to investigate the charge storage mechanisms on the three couple of redox reactions, the ex-situ XPS tests were carried out (Figure S6, S7 and S8). And the corresponding valence variation of Mn and

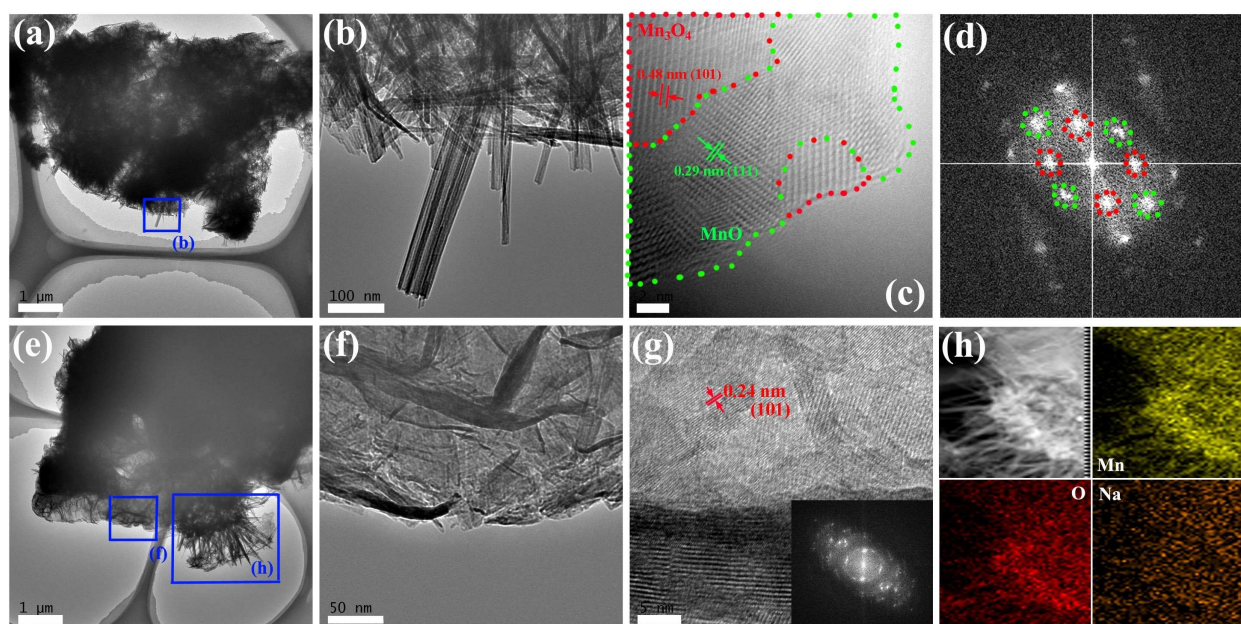


**Figure 2.** (a) TEM image, (b) partial enlarged TEM image, (c) high-resolution TEM image (scale bar is 2 nm) and (d) corresponding fast Fourier transform (FFT) for  $\text{MnO}/\text{Mn}_3\text{O}_4$ . (e) TEM image, (f) partial enlarged TEM image, (g) high-resolution TEM image (scale bar is 5 nm, inset: FFT) and (h) HADDF-STEM image of Mn, O and Na elements for  $\text{Na}_{0.91}\text{MnO}_2$ .

the relative content change of Na ( $\text{Na}^+$ ) vs Mn are recorded (Figure 3b). The ratio of  $\text{Mn}^{3+}/\text{Mn}^{4+}$  first decreases for the charge process and then increases for the discharge process accompanied with the variations of Na with the same change as the one of  $\text{Mn}^{3+}/\text{Mn}^{4+}$ . Specifically, the redox peaks of R1 at 0.15 V and R6 at  $-0.18$  V are due to Faradaic reaction between  $\text{Mn}^{3+}$  and  $\text{Mn}^{4+}$  accompanied with the insertion/extraction of  $\text{Na}^+$  (Figure 3b). For redox peaks of R2 at 0.62 V and R5 at 0.55 V, the current response originates from the reversible transition of  $\text{Mn}^{3+}/\text{Mn}^{4+}$  and the insertion/extraction of  $\text{Na}^+$ , which is consistent with the reported literature.<sup>[21]</sup> The current response of peak R3 at 1 V and peak R4 at 0.85 V also consists of the reversible transition of  $\text{Mn}^{3+}/\text{Mn}^{4+}$  and the insertion/extraction of  $\text{Na}^+$  consistent with the reported literature of  $\text{Na}_{0.5}\text{MnO}_2$ , indicating the partial extraction of  $\text{Na}^+$  while the potential limit is below 1 V.<sup>[12]</sup> Interestingly, the relative content of O anion (O1 vs Mn2p) also shows the increase and then the decrease during charging/discharging process (Figure S9 and Table S1), indicating O anion contributes to the total capacity. Recently, Ling *et. al.* also reports the O anion contribute to the capacity in cobalt oxide.<sup>[39]</sup> While the scan rates increase up to  $100 \text{ mVs}^{-1}$  from  $20 \text{ mVs}^{-1}$  (Figure 3c), the peak current response from the charge process (from  $-0.6$  V to 1.2 V) also enhances with the positive shift of the peak potential. During the anodic scans (from 1.2 V to  $-0.6$  V), the current response of R4 peaks becomes more pronounced compared to R5 and R6 peaks, indicating the increased capacity contribution of R4 peaks to the total capacity. Trasatti's method is used to separate the capacity contribution from the surface and the diffusion processes.<sup>[40,41]</sup> The gravimetric capacity as a function of the inverse square root of scan rate and the linear fit were done (Figure S10). The surface capacity is obtained by extrapolating to the rate-independent limit. The contributions of the surface and diffusion-controlled capacities to the total capacity of  $\text{Na}_{0.91}\text{MnO}_2$  at the different scan rates are separated (Figure 3d). The calculated surface capacity is about 36% of the total capacity at the low scan rate of  $10 \text{ mVs}^{-1}$ , lower than that of the diffusion controlled one, demonstrating the dominant diffusion-controlled charge storage behavior for  $\text{Na}_{0.91}\text{MnO}_2$  electrode. The diffusion-controlled capacity gradually decreases with the increased scan rates, resulting in the decreased total capacity. The galvanostatic charge/discharge (GCD) curves of  $\text{Na}_{0.91}\text{MnO}_2$  electrode shows the wide potential window of  $-0.6$  V to 1.2 V at different current densities (Figure 3e). For the electrode materials testing in a three-electrode system, only a fraction of an RC time constant upon current interruption is reached, resulting in an obvious IR drop (Figure 3e).<sup>[42]</sup> The specific capacity of  $\text{Na}_{0.91}\text{MnO}_2$  electrode as a function of current density is recorded (Figure 3f). The specific capacity of  $\text{Na}_{0.91}\text{MnO}_2$  electrode is up to  $856 \text{ C g}^{-1}$  ( $476 \text{ F g}^{-1}$ ) at the current density of  $1 \text{ A g}^{-1}$ , higher than that of the reported capacities on  $\text{MnO}_2$  electrode materials in literatures (Table S2) and the capacity of the prepared  $\text{MnO}/\text{Mn}_3\text{O}_4$  (Figure S11). To investigate the stability of the prepared electrodes, the long-term cycle in the potential window of  $-0.6$  V to 1.2 V was tested (Figure 3g). The two type of electrodes show 100% of the coulombic efficiency. After 10000 cycles,  $\text{MnO}/\text{Mn}_3\text{O}_4$  electrode exhibits significant capacity degradation only with 42% of capacity retention at a low current density of  $35 \text{ A g}^{-1}$ . The rapid degradation of the capacity in the initial 650 cycles is due to the dissolution of  $\text{Mn}^{2+}$  into electrolyte derived from Jahn-Teller effect.<sup>[29]</sup> Surprisingly,  $\text{Na}_{0.91}\text{MnO}_2$  electrode shows no capacity degradation after 10000 cycles even at the same current density, indicative of an excellent stability.

olating to the rate-independent limit. The contributions of the surface and diffusion-controlled capacities to the total capacity of  $\text{Na}_{0.91}\text{MnO}_2$  at the different scan rates are separated (Figure 3d). The calculated surface capacity is about 36% of the total capacity at the low scan rate of  $10 \text{ mVs}^{-1}$ , lower than that of the diffusion controlled one, demonstrating the dominant diffusion-controlled charge storage behavior for  $\text{Na}_{0.91}\text{MnO}_2$  electrode. The diffusion-controlled capacity gradually decreases with the increased scan rates, resulting in the decreased total capacity. The galvanostatic charge/discharge (GCD) curves of  $\text{Na}_{0.91}\text{MnO}_2$  electrode shows the wide potential window of  $-0.6$  V to 1.2 V at different current densities (Figure 3e). For the electrode materials testing in a three-electrode system, only a fraction of an RC time constant upon current interruption is reached, resulting in an obvious IR drop (Figure 3e).<sup>[42]</sup> The specific capacity of  $\text{Na}_{0.91}\text{MnO}_2$  electrode as a function of current density is recorded (Figure 3f). The specific capacity of  $\text{Na}_{0.91}\text{MnO}_2$  electrode is up to  $856 \text{ C g}^{-1}$  ( $476 \text{ F g}^{-1}$ ) at the current density of  $1 \text{ A g}^{-1}$ , higher than that of the reported capacities on  $\text{MnO}_2$  electrode materials in literatures (Table S2) and the capacity of the prepared  $\text{MnO}/\text{Mn}_3\text{O}_4$  (Figure S11). To investigate the stability of the prepared electrodes, the long-term cycle in the potential window of  $-0.6$  V to 1.2 V was tested (Figure 3g). The two type of electrodes show 100% of the coulombic efficiency. After 10000 cycles,  $\text{MnO}/\text{Mn}_3\text{O}_4$  electrode exhibits significant capacity degradation only with 42% of capacity retention at a low current density of  $35 \text{ A g}^{-1}$ . The rapid degradation of the capacity in the initial 650 cycles is due to the dissolution of  $\text{Mn}^{2+}$  into electrolyte derived from Jahn-Teller effect.<sup>[29]</sup> Surprisingly,  $\text{Na}_{0.91}\text{MnO}_2$  electrode shows no capacity degradation after 10000 cycles even at the same current density, indicative of an excellent stability.

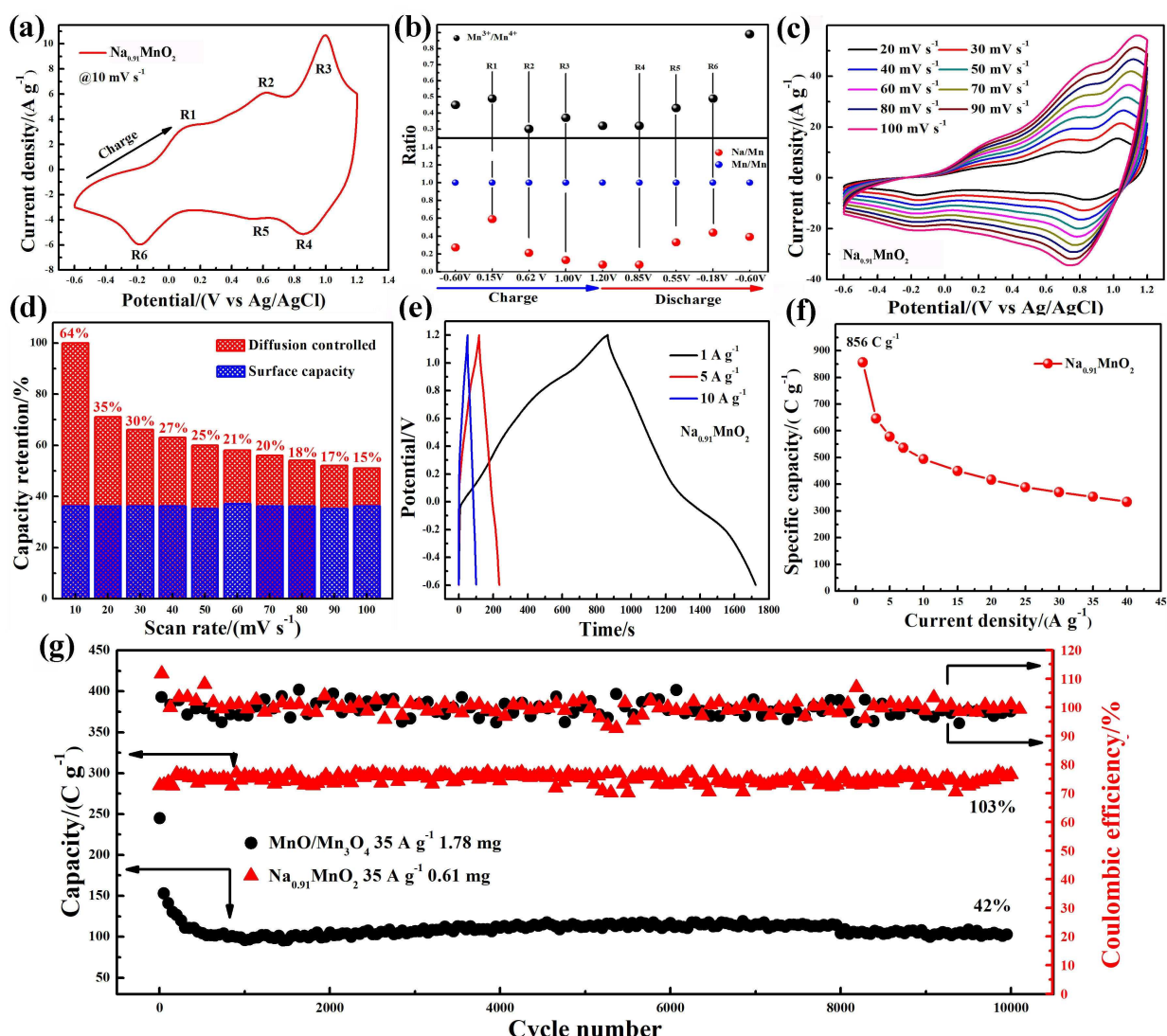


**Figure 3.** (a) CV curve at  $10 \text{ mV s}^{-1}$  for  $\text{Na}_{0.91}\text{MnO}_2$  on an ECC electrode. (b) The valence variation of Mn and the relative content change of Na to Mn at different charge/discharge states for a CV test at  $10 \text{ mV s}^{-1}$ . (c) CV curves at high scan rates for  $\text{Na}_{0.91}\text{MnO}_2$  on an ECC electrode. (d) Separations of diffusion-controlled and capacitive charge at different scan rates. (e) GCD curves and (f) specific capacity as a function of current density for  $\text{Na}_{0.91}\text{MnO}_2$  on an ECC electrode. (g) Long-term cycle stability test of  $\text{Na}_{0.91}\text{MnO}_2$  and  $\text{MnO}/\text{Mn}_3\text{O}_4$  on ECC electrodes.

The electrochemical performances of aqueous supercapacitor based on  $\text{Na}_{0.91}\text{MnO}_2$  or  $\text{MnO}/\text{Mn}_3\text{O}_4$  cathode and Na–CC anode ( $\text{Na}^+$  modified carbon cloth) are characterized using the two-electrode systems to demonstrate the ability of  $\text{Na}_{0.91}\text{MnO}_2$  cathode to operate in a wide potential window of 1.8 V or wider (Figure 4), in which the corresponding characterizations of Na–CC are carried out (Figure S12). Na–CC shows the high areal capacity in the three-electrode system (Figure S12g) but almost no capacity contribution to Na–CC// $\text{Na}_{0.91}\text{MnO}_2$  (Figure S13), which plays the role of the counter and reference electrodes. CV curves of Na–CC// $\text{Na}_{0.91}\text{MnO}_2$  show three couple of redox peaks within the potential window of 0 V to 2.07 V (Figure 4a). The variation of the peak current response presents the same variation trend as the three-electrode system. GCD curves of Na–CC// $\text{Na}_{0.91}\text{MnO}_2$  at the different current densities were collected within the potential window of 0 to 2.07 V

(Figure 4b). For the supercapacitor in a charge/discharge process, only a fraction of an RC time constant upon current interruption is reached, resulting in an obvious IR drop (Figure 4b).<sup>[42]</sup> The specific capacitance as a function of current density is recorded (Figure 4c). At the current density of  $1 \text{ A g}^{-1}$ , the aqueous supercapacitor of Na–CC// $\text{Na}_{0.91}\text{MnO}_2$  can deliver a high capacity of  $482 \text{ C g}^{-1}$  based on the active materials of  $\text{Na}_{0.91}\text{MnO}_2$ , higher than that of the aqueous supercapacitor of Na–CC// $\text{MnO}/\text{Mn}_3\text{O}_4$  (Figure S14).  $202 \text{ C g}^{-1}$  of specific capacity is retained even at a high current density of  $32 \text{ A g}^{-1}$ , indicating the superior charge storage ability for Na–CC// $\text{Na}_{0.91}\text{MnO}_2$ . Based on GCD curves at different current densities, the energy and power densities for Na–CC// $\text{Na}_{0.91}\text{MnO}_2$  and Na–CC// $\text{MnO}/\text{Mn}_3\text{O}_4$  are displayed in Ragone plots (Figure 4d). The aqueous supercapacitor of Na–CC// $\text{Na}_{0.91}\text{MnO}_2$  shows the maximum energy density of  $138 \text{ Wh kg}^{-1}$  higher than that of  $106 \text{ Wh kg}^{-1}$

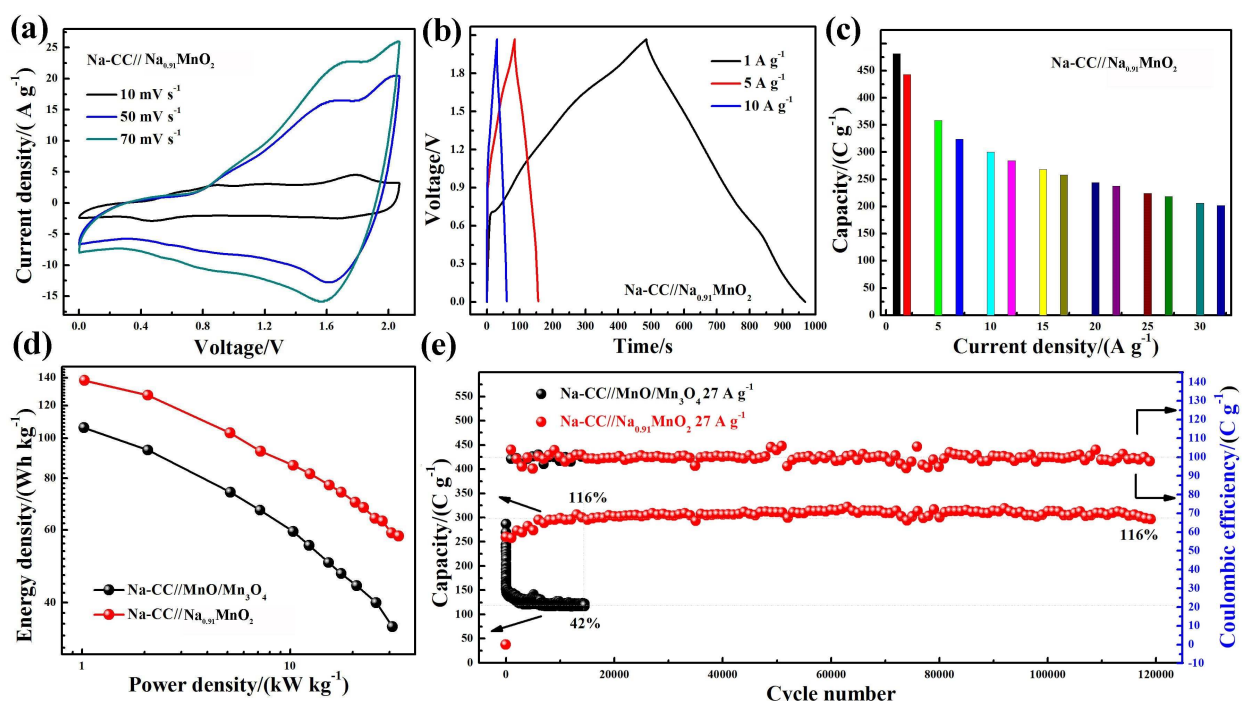


**Figure 4.** (a) CV curves, (b) GCD curves and (c) the capacity as a function of current density for Na-CC//Na<sub>0.91</sub>MnO<sub>2</sub>. (d) Ragone plots and (d) long-term cycle stability and coulombic efficiency of Na-CC//MnO/Mn<sub>3</sub>O<sub>4</sub> and Na-CC//Na<sub>0.91</sub>MnO<sub>2</sub>.

of Na-CC//MnO/Mn<sub>3</sub>O<sub>4</sub> and the values of MnO<sub>2</sub>-based supercapacitors (Table S3). Na-CC//Na<sub>0.91</sub>MnO<sub>2</sub> can still exhibit a high energy density of 58 Wh kg<sup>-1</sup> even at a high power density of 33 kW kg<sup>-1</sup>, which is superior to Na-CC//MnO/Mn<sub>3</sub>O<sub>4</sub> of 35 Wh kg<sup>-1</sup> at a high power density of 31 kW kg<sup>-1</sup>. And the aqueous supercapacitor of Na-CC//Na<sub>0.91</sub>MnO<sub>2</sub> also presents an excellent cycling stability with the wide voltage window of 0~2.07 V. Na-CC//Na<sub>0.91</sub>MnO<sub>2</sub> and Na-CC//MnO/Mn<sub>3</sub>O<sub>4</sub> displays 100% of coulombic efficiency after 120000 cycles (Figure 4e). At the current density of 27 A g<sup>-1</sup>, Na-CC//MnO/Mn<sub>3</sub>O<sub>4</sub> shows obvious capacity degradation only with ~42% of retention of the initial capacity after 14000 cycles due to the dissolution of Mn<sup>2+</sup>.<sup>29</sup> Surprisingly, Na-CC//Na<sub>0.91</sub>MnO<sub>2</sub> exhibits no capacity deterioration with 116% of retention of the initial capacity after 14000 and even 120000 cycles at a higher current density of 27 A g<sup>-1</sup>, indicative of an outstanding cycling stability. The excellent cycling stability of Na-CC//Na<sub>0.91</sub>MnO<sub>2</sub> is comparable to the electrochemical capacitors with the charge storage mechanism of the electric double layer and promising for the practical applications.<sup>[21]</sup>

### 3. Conclusion

Tetragonal phase of Na<sub>0.91</sub>MnO<sub>2</sub> nano-sheet arrays were in-situ formed on the electrochemically treated carbon cloth (ECC) by the transition of face-centered cubic phase MnO/hausmannite phase Mn<sub>3</sub>O<sub>4</sub> based on Jahn-Teller effect. The face-centered cubic/hausmannite phases were converted into tetragonal phase by the simple electrochemical oxidation method accompanied by Na<sup>+</sup> insertion between crystal layers. It was observed

that Na<sub>0.91</sub>MnO<sub>2</sub> nano-sheet arrays electrode can operate stably within the potential window from -0.6 V to 1.2 V (vs Ag/AgCl) with ultrahigh capacity of 856 C g<sup>-1</sup> and no capacity degradation after 10000 cycles as well as excellent rate ability. The outstanding properties are due to three couple of redox reactions, high cations content and hierarchical structure. With the heteroatom-rich mesopore carbon fiber fabric of Na-CC as anode (counter and reference electrodes), a two-electrode cell configuration based on Na<sub>0.91</sub>MnO<sub>2</sub> as cathode and Na-CC is employed to further demonstrate the advantage of the wide potential window. It is more surprising that Na<sub>0.91</sub>MnO<sub>2</sub> nano-sheet arrays can operate stably within the voltage range from 0 to 2.07 V also with three couple of redox peaks, delivering the high energy density of 138 Wh kg<sup>-1</sup> and the excellent power density 33 kW kg<sup>-1</sup> based on the active material of Na<sub>0.91</sub>MnO<sub>2</sub>. Moreover, 100% retention of the initial capacity is obtained after 120000 cycles at a high current density of 27 A g<sup>-1</sup>. This work may pave the way for the development of aqueous supercapacitor cathode with the wide potential window.

### Experimental Section

#### Fabrication of the Electrochemically Treated Carbon Cloth (ECC)

Low surface area carbon cloth (CC, 3×3 cm<sup>-2</sup>) purchased from Tanneng of Taiwan was treated by the simple electrochemical treatment in a three-electrode configuration with the constant potential of 3 V (vs SCE) and 15 minutes to increase O content, in which 60 mL concentrated sulfuric acid was selected as electrolyte and Pt plate as counter electrode. Then, CC was washed with the

amount of deionized water and dried at 60 °C in an oven overnight. The electrochemical treated carbon cloth is denoted as ECC.

### Preparation of $\text{Na}_{0.91}\text{MnO}_2$ Nanosheet Arrays on ECC

$\text{MnO}/\text{Mn}_3\text{O}_4$  nanowires assembled nanosheets were electrodeposited on ECC using the chronoamperometry technique (electrochemical station CHI660E). For the electro-deposition for  $\text{MnO}/\text{Mn}_3\text{O}_4$ , a mixed solution containing 0.1 M  $\text{Mn}(\text{CH}_3\text{COO})_2$  and 0.1 M  $\text{Na}_2\text{SO}_4$  was used as electrolyte. The electro-deposition was conducted in a three-electrode configuration composed of ECC ( $1.1 \times 1.5 \text{ cm}^2$ ) as the working electrode (WE) with the part ( $1.1 \times 1 \text{ cm}^2$ ) immersed in electrolyte, Pt plate as counter electrode (CE) and Ag/AgCl electrode as reference electrode (RE). A constant potential of  $-1.8 \text{ V}$  was applied to start the electro-deposition process for 4 minutes at  $21^\circ\text{C}$  to get the precursor. The precursor was washed with the amount of deionized water and dried at room temperature overnight, in which the precursor oxides automatically into  $\text{MnO}/\text{Mn}_3\text{O}_4$  on ECC.

The final  $\text{Na}_{0.91}\text{MnO}_2$  nanosheets/nanowires arrays on ECC were gained by the simple electrochemical oxidation method including the cyclic voltammetry (CV) and the chronopotentiometry (GCD). Firstly,  $\text{MnO}/\text{Mn}_3\text{O}_4$  on ECC was treated using CV within the potential range from 0 V to  $1.3 \text{ V}$  (vs Ag/AgCl), in which the scan rate of  $80 \text{ mV s}^{-1}$  is selected to start CV process with 510 cycles in 1 M  $\text{Na}_2\text{SO}_4$  aqueous electrolyte. The sample is washed with the amount of deionized water and dried at room temperature overnight. Then, GCD was employed to stable the sample treated by CV, in which the current density of  $35 \text{ A g}^{-1}$  is selected to initiate GCD process within the potential window of  $-0.6 \text{ V}$  to  $1.2 \text{ V}$  (vs Ag/AgCl) with 10000 cycles in 1 M  $\text{Na}_2\text{SO}_4$  aqueous electrolyte. The final  $\text{Na}_{0.91}\text{MnO}_2$  nanosheets/nanowires arrays on ECC was washed with the amount of deionized water and dried at room temperature overnight. The mass loading of  $\text{MnO}/\text{Mn}_3\text{O}_4$  and  $\text{Na}_{0.91}\text{MnO}_2$  are  $1.78 \text{ mg cm}^{-2}$  and  $0.61 \text{ mg cm}^{-2}$  according the mass variation of ECC before and after the electro-deposition and the electrochemical oxidation method, respectively.

### Preparation of Na–CC Anode (Counter and Reference Electrodes)

Carbon fiber fabric with large surface area (Shanghai Lishuo Composite Material Technology Co., Ltd; denoted as CC,  $1 \times 1 \text{ cm}^2$ ) was treated by the simple CV method in a three-electrode configuration with the potential range from 0 V to  $-1.5 \text{ V}$  (vs Ag/AgCl) in 1 M  $\text{Na}_2\text{SO}_4$  aqueous solution with the volume of 60 mL. Pt plate was used as the counter electrode. Firstly, the scan rate of  $25 \text{ mV s}^{-1}$  was selected to start CV process for 100 cycles. Then, the scan rate of  $10 \text{ mV s}^{-1}$  was used to continue CV process for 300 cycles with another cup of 1 M  $\text{Na}_2\text{SO}_4$  aqueous solution with the volume of 60 mL. The final sample (Na–CC) was washed with the amount of deionized water and dried at room temperature overnight.

### Characterization

The morphologies and their variations of the as-prepared samples were observed by field emission scanning electron microscopy (FE-SEM, Hitachi S-4800) and transmission electron microscopy (TEM, FEI Tecnai F30, operated at 300 kV). The crystal structure of the samples was determined using X-ray diffraction (XRD, Cu K $\alpha$  irradiation;  $\lambda = 0.15418 \text{ nm}$ ) with a SIEMENS D5000 X-ray diffractometer. Nitrogen adsorption/desorption is carried out at  $77 \text{ K}$  on ASAP 2027 specific surface area and pore diameter analyzer and

sample was degassed at  $200^\circ\text{C}$  for 6 h under vacuum prior to the measurement. The chemical component was analyzed on a multi-functional X-ray photoelectron spectroscope (XPS, PHI-5702, Mg K $\alpha$  X-ray, 1253.6 eV).

### Electrochemical Measurements

Electrochemical properties tests of the as-prepared samples in the experiment were conducted in a three-electrode configuration with 1 M of  $\text{Na}_2\text{SO}_4$  electrolyte and Ag/AgCl as reference electrode at room temperature. CV and GCD of single electrode were tested in the electrochemical station (CHI660E). The electrochemical impedance spectroscopy (EIS) measurements were obtained at open circuit potential with the frequency ranging from 100 kHz to 10 mHz at an amplitude of 5 mV. The long-term cycle was carried out by GCD measurements. The capacitances were calculated from GCD curves for  $\text{MnO}/\text{Mn}_3\text{O}_4$  and  $\text{Na}_{0.91}\text{MnO}_2$  cathode according to the formula:  $C = I\Delta t / (Cg^{-1})$ , where  $I$  is the constant discharge current density ( $\text{A g}^{-1}$ ) and  $\Delta t$  the discharge time (s). The energy densities were obtained according to  $E = CV^2/7.2$ . And the power density was obtained according to  $P = E \times 3600/\Delta t$ . The capacitances for Na–CC anode were calculated from GCD curves according to the formula:  $C_A = (I\Delta t)/(S\Delta V)$ , where  $S$  the area of device,  $\Delta V$  voltage drop upon discharging and  $C_A$  areal capacitance.

### Acknowledgements

This work was financially supported by the Fundamental Research Funds for the Central Universities (No. Izujbky-2019-it23). Thank the Clean energy materials and devices laboratory for providing the experiment conditions that guarantees the work accomplished.

### Conflict of Interest

The authors declare no conflict of interest.

**Keywords:** cation insertion • manganese oxides • redox reactions • supercapacitor cathode • voltage window

- [1] P. Simon, Y. Gogotsi, *Nat. Mater.* **2008**, *7*, 845–854.
- [2] C. Zhong, Y. Deng, W. Hu, J. Qiao, L. Zhang, J. Zhang, *Chem. Soc. Rev.* **2015**, *44*, 7484–7539.
- [3] J. Yan, Q. Wang, T. Wei, Z. Fan, *Adv. Energy Mater.* **2014**, *4*, 1300816.
- [4] Y. Han, Y. Lu, S. Shen, Y. Zhong, S. Liu, X. Xia, Y. Tong, X. Lu, *Adv. Funct. Mater.* **2019**, *29*, 1806329.
- [5] X. Xia, Y. Zhang, Z. Fan, D. Chao, Q. Xiong, J. Tu, H. Zhang, H. J. Fan, *Adv. Energy Mater.* **2015**, *5*, 1401709.
- [6] X. Xia, Y. Zhang, D. Chao, Q. Xiong, Z. Fan, X. Tong, J. Tu, H. Zhang, H. J. Fan, *Energy Environ. Sci.* **2015**, *8*, 1559–1568.
- [7] Y. Zhang, X. Xia, B. Liu, S. Deng, D. Xie, Q. Liu, Y. Wang, J. Wu, X. Wang, J. Tu, *Adv. Energy Mater.* **2019**, *9*, 1803342.
- [8] W. Zuo, C. Xie, P. Xu, Y. Li, J. Liu, *Adv. Mater.* **2017**, *29*, 1703463.
- [9] L. Suo, O. Borodin, W. Sun, X. Fan, C. Yang, F. Wang, T. Gao, Z. Ma, M. Schroeder, A. von Cresce, S. M. Russell, M. Armand, A. Angell, K. Xu, C. Wang, *Angew. Chem.* **2016**, *55*, 7136–7141.
- [10] Q. Dou, S. Lei, D.-W. Wang, Q. Zhang, D. Xiao, H. Guo, A. Wang, H. Yang, Y. Li, S. Shi, X. Yan, *Energy Environ. Sci.* **2018**, *11*, 3212–3219.
- [11] L. Suo, O. Borodin, T. Gao, M. Olgun, J. Ho, X. Fan, C. Luo, C. Wang, K. Xu, *Science* **2015**, *350*, 938–943.
- [12] N. Jabeen, A. Hussain, Q. Xia, S. Sun, J. Zhu, H. Xia, *Adv. Mater.* **2017**, *29*, 1700804.

- [13] R. Li, Y. Wang, C. Zhou, C. Wang, X. Ba, Y. Li, X. Huang, J. Liu, *Adv. Funct. Mater.* **2015**, *25*, 5384–5394.
- [14] S. Liu, G. L. Pan, N. F. Yan, X. P. Gao, *Energy Environ. Sci.* **2010**, *3*, 1732–1735.
- [15] A. J. Paleo, P. Staiti, A. Brigandì, F. N. Ferreira, A. M. Rocha, F. Lufrano, *Energy Storage Mater.* **2018**, *12*, 204–215.
- [16] C. Xu, F. Kang, B. Li, H. Du, *J. Mater. Res.* **2011**, *25*, 1421–1432.
- [17] S. Zhu, L. Li, J. Liu, H. Wang, T. Wang, Y. Zhang, L. Zhang, R. S. Ruoff, F. Dong, *ACS Nano* **2018**, *12*, 1033–1042.
- [18] P. R. Deshmukh, Y. Sohn, W. G. Shin, *Electrochim. Acta* **2018**, *285*, 381–392.
- [19] T. Qin, B. Liu, Y. Wen, Z. Wang, X. Jiang, Z. Wan, S. Peng, G. Cao, D. He, *J. Mater. Chem. A* **2016**, *4*, 9196–9203.
- [20] Y. Wen, T. Qin, Z. Wang, X. Jiang, S. Peng, J. Zhang, J. Hou, F. Huang, D. He, G. Cao, *J. Alloys Compd.* **2017**, *699*, 126–135.
- [21] T. Xiong, T. L. Tan, L. Lu, W. S. V. Lee, J. Xue, *Adv. Energy Mater.* **2018**, *8*, 1702630.
- [22] R. Jia, F. Zhu, S. Sun, T. Zhai, H. Xia, *J. Power Sources* **2017**, *341*, 427–434.
- [23] L. Athouël, F. Moser, R. Dugas, O. Crosnier, D. Bélanger, T. Brousse, *J. Phys. Chem. C* **2008**, *112*, 7270–7277.
- [24] A. Boisset, L. Athouël, J. Jacquemin, P. Porion, T. Brousse, M. Anouti, *J. Phys. Chem. C* **2013**, *117*, 7408–7422.
- [25] X. Wei, H. Peng, Y. Li, Y. Yang, S. Xiao, L. Peng, Y. Zhang, P. Xiao, *ChemSusChem* **2018**, *11*, 3167–3174.
- [26] X. F. Lu, Z. X. Huang, Y. X. Tong, G. R. Li, *Chem. Sci.* **2016**, *7*, 510–517.
- [27] M. J. Young, M. Neuber, A. C. Cavanagh, H. Sun, C. B. Musgrave, S. M. George, *J. Electrochem. Soc.* **2015**, *162*, A2753–A2761.
- [28] X. Shan, D. S. Charles, W. Xu, M. Feygenson, D. Su, X. Teng, *Adv. Funct. Mater.* **2017**, *28*, 1703266.
- [29] H. J. Lee, J. Shin, J. W. Choi, *Adv. Mater.* **2018**, *30*, e1705851.
- [30] Y. Chu, L. Guo, B. Xi, Z. Feng, F. Wu, Y. Lin, J. Liu, D. Sun, J. Feng, Y. Qian, S. Xiong, *Adv. Mater.* **2018**, *30*, 1704244.
- [31] J. Huang, J. Luo, *Sci. Chin. Technol. Sci.* **2016**, *59*, 1042–1047.
- [32] C. Julien, *Solid State Ionics* **2003**, *159*, 345–356.
- [33] X. Chen, X. Li, Y. Jiang, C. Shi, X. Li, *Solid State Commun.* **2005**, *136*, 94–96.
- [34] H. Xia, M. Lai, L. Lu, *J. Mater. Chem.* **2010**, *20*, 6896–6902.
- [35] N. Yu, H. Yin, W. Zhang, Y. Liu, Z. Tang, M.-Q. Zhu, *Adv. Energy Mater.* **2016**, *6*, 1501458.
- [36] J. Gu, Y. Gu, S. Yang, *Chem. Commun.* **2017**, *53*, 12642–12645.
- [37] B. Patil, S. Ahn, S. Yu, H. Song, Y. Jeong, J. H. Kim, H. Ahn, *Carbon* **2018**, *134*, 366–375.
- [38] Y. Zeng, Z. Lai, Y. Han, H. Zhang, S. Xie, X. Lu, *Adv. Mater.* **2018**, e1802396.
- [39] T. Ling, P. Da, X. Zheng, B. Ge, Z. Hu, M. Wu, X.-W. Du, W.-B. Hu, M. Jaroniec, S.-Z. Qiao, *Sci. Adv.* **2018**, *4*, eaau6261.
- [40] J. Liu, J. Wang, C. Xu, H. Jiang, C. Li, L. Zhang, J. Lin, Z. X. Shen, *Adv. Sci.* **2018**, *5*, 1700322.
- [41] V. Augustyn, J. Come, M. A. Lowe, J. W. Kim, P. L. Taberna, S. H. Tolbert, H. D. Abruna, P. Simon, B. Dunn, *Nat. Mater.* **2013**, *12*, 518–522.
- [42] S. Zhao, F. Wu, L. Yang, L. Gao, A. F. Burke, *Electrochim. Commun.* **2010**, *12*, 242–245.

Manuscript received: July 13, 2019

Revised manuscript received: August 15, 2019

Accepted manuscript online: August 16, 2019

Version of record online: September 11, 2019